Nano Energy 74 (2020) 104876

Contents lists available at ScienceDirect

Nano Energy

journal homepage: http://www.elsevier.com/locate/nanoen

Epitaxial array of Fe_3O_4 nanodots for high rate high capacity conversion type lithium ion batteries electrode with long cycling life

Gaokuo Zhong [a,1], Ke Qu [a,b,1], Chuanlai Ren [a,c,1], Yong Su [c], Bi Fu [a], Mengfei Zi [a,c], Liyufen Dai [a,c], Qun Xiao [a,c], Jun Xu [d], Xiangli Zhong [c], Feng An [a,c], Mao Ye [e], Shanming Ke [f], Shuhong Xie [c], Jinbin Wang [c], Peng Gao [b,d,**], Jiangyu Li [a,*]

[a] Shenzhen Key Laboratory of Nanobiomechanics, Shenzhen Institutes of Advanced Technology, Chinese Academy of Sciences, Shenzhen, China
[b] Electron Microscopy Laboratory, School of Physics, Peking University, Beijing, China
[c] School of Materials Science and Engineering, Xiangtan University, Xiangtan, China
[d] International Center for Quantum Materials, Peking University, Beijing, China
[e] Department of Physics, Southern University of Science and Technology, Shenzhen, China
[f] School of Materials Science and Engineering, Nanchang University, Nanchang, China

ARTICLE INFO

Keywords:
Lithium ion batteries
Epitaxial oxide
Fe3O4
Pulsed laser deposition

ABSTRACT

With the energy density of intercalation electrodes approaching the ceiling, there are tremendous interests in developing metal oxide conversion type electrodes for lithium ion batteries, which involve more lithium ions in electrochemical reactions. Nevertheless, the cyclic and rate performances of conversion electrodes are rather poor, due to their large volume changes during charging and discharging, poor contact with current collector, and accumulated internal passivation over cycling. Here by carefully designing epitaxial array of Fe_3O_4 nanodots as a binder-free conversion electrode, we accomplish excellent rate performance under current density as high as 60C with long cycling life and good capacity, and the detailed scanning transmission electron microscopy in combination with comprehensive electrochemical analysis suggest that the success can be attributed to the synergic effects of released internal stress, slowed internal passivation, and good structure integrity all rendered by the nanodot array architecture of Fe_3O_4. Our study thus overcome materials breakdown, contact failure, and internal passivation of conventional conversion electrodes, providing new insight into optimizing conversion electrodes for practical applications.

1. Introduction

The commercial success of lithium ion batteries (LIBs) is largely built on intercalation type electrode materials such as lithium transition metal oxides [1,2], though the number of lithium ions that can be reversibly inserted and extracted is limited, and the corresponding energy density is approaching the ceiling [3]. There are thus tremendous interests in developing conversion type electrodes such as metal oxides for LIBs [4–6], which involve more lithium ions in electrochemical reactions, and therefore promise much higher specific capacities. Nevertheless, the conversion electrodes often suffer from rapid capacity decay under cycling [7], and their rate performance under high current is rather poor [8], severely limiting their practical applications. Much effort thus has been devoted to understand the electrochemical process of conversion electrodes during charging and discharging, for example in Fe_3O_4, wherein the microstructure evolution has been extensively investigated [9–11].

Fe_3O_4 is one of the earliest conversion electrodes studied, pioneered by Thackeray and Goodenough in early 1980s [12], who uncovered two-step lithiation process of intercalation and conversion. They concluded that "*Fe_3O_4 must therefore be regarded as attractive candidates for use in high energy-density batteries*" [13], with a theoretical capacity of 926 mA h/g [14], though this potential has yet to be practically realized. On one hand, the typical issue of volume changes during charging and discharging is substantial, as high as 100% for Fe_3O_4 [15,16], resulting in large deformation and internal stress and thus poor reliability. On the

* Corresponding author.
** Corresponding author. Electron Microscopy Laboratory, School of Physics, Peking University, Beijing, China.
E-mail addresses: p-gao@pku.edu.cn (P. Gao), jy.li1@siat.ac.cn (J. Li).
[1] These authors contributed equally to this work.

https://doi.org/10.1016/j.nanoen.2020.104876
Received 5 March 2020; Received in revised form 9 April 2020; Accepted 20 April 2020
Available online 4 May 2020

other hand, it is also recently revealed that accumulation of internal passivation phase is significant [17], resulting in further capacity decay upon cycling and poor rate performance. The latter effect probably explains only limited success of nanocomposite electrodes based on Fe_3O_4 despite extensive researches, especially on the rate performance [18–21]. Nevertheless, recent study also demonstrated that the cubic close packed oxygen-anion framework of Fe_3O_4 is retained upon lithiation, despite conventional belief that the crystalline structure of electrode would collapse during conversion process [22], rendering hope that the poor cycling performance of Fe_3O_4, especially under high current rate, can be mitigated. Indeed, by carefully designing epitaxial array of Fe_3O_4 nanodots as a binder-free electrode, we accomplish excellent rate performance under current density as high as 60C with long cycling life and good capacity, and the success can be attributed to synergic effects of released internal stress, slowed internal passivation, and good structure integrity all rendered by the nanodot array architecture.

2. Results

Fe_3O_4 crystallizes in cubic inverse spinel structure, as schematically shown in the left panel of Fig. 1a, with one unit cell containing 64 oxygen tetrahedrons and 32 oxygen octahedrons [23]. At the first stage of lithium intercalation, as visualized in the right panel of Fig. 1a, the ferric irons in the oxygen tetrahedron is evolved into ferrous irons [12]. With further lithiation, the oxygen tetrahedrons and oxygen tetrahedrons in Fe_3O_4 are gradually occupied by lithium ions, and the structure is eventually evolved to form Li_2O and Fe [24]. The theoretical capacity is thus calculated to be as high as 926 mA h/g [14], though the processes of charging and discharging are found to be highly irreversible, making cycling very challenging for LIBs [25]. To overcome such difficulty, Li-ion battery based on Fe_3O_4 array is designed as illustrated in Fig. 1b, with which we hope that the structure stability can be maintained during charging and discharging, and the reversibility of the battery can be improved. We thus produce epitaxial Fe_3O_4 array on Cu foil via pulse laser deposition (PLD) in combination with anodic aluminum oxide (AAO) template [26], which we believe can improve the quality of Fe_3O_4 array substantially. The process is schematically shown in Fig. 1c, consisting of mask transfer, Fe_3O_4 deposition, and mask removal steps. The morphologies of deposited Fe_3O_4 array before and after mask removal are examined by top-view scanning electronic microscopy (SEM) shown in Fig. 1d and e, revealing ordered array of Fe_3O_4 nanodots of approximately 130 nm radius with uniform space of about 200 nm. Nanodots with different radius of 45 nm and 175 nm are also successfully fabricated, as shown in Fig. S1 in the Supplementary Information (SI), illustrating high fidelity fabrication of ordered Fe_3O_4 array vertically grown on Cu foil as designed.

The structure of as-deposited Fe_3O_4 is further examined by cross-sectional scanning transmission electron microscopy (STEM) image in Fig. 2a, revealing two nanodots of pyramid shape with thickness of ~256 nm on the substrate. The corresponding energy dispersive spectroscopy (EDS) mappings in Fig. 2a exhibit uniform distribution of Fe and O within nanodots, connected by a thin layer of iron oxide of approximately 35 nm in thickness on top of Cu foil. The detailed atomic structure of a representative Fe_3O_4 nanodot with corresponding interface with Cu is examined by high angle annular dark field mode (HAADF) in Fig. 2b, exhibiting excellent crystallinity that matches cubic inverse spinel structure well. The epitaxial growth of Fe_3O_4 can be clearly revealed by well-matched HAADF-STEM image and structural models at selected region of Cu–Fe_3O_4 interface in Fig. 2c, and the epitaxial relationship of Fe_3O_4 nanodot and Cu substrate is determined to be Fe_3O_4 [111]//Cu [011]. The Cu–Fe_3O_4 interfaces in Fig. 2a–c are found to be clean and sharp, demonstrating the high quality deposition of Fe_3O_4 and excellent contact between Fe_3O_4 and Cu, critical for its battery applications. The phase structure of Fe_3O_4 is further examined by X-ray photoelectron spectroscopy (XPS), as shown in Fig. 2d, wherein two peaks located at around 724.2 eV and 711 eV correspond to Fe $2p_{1/2}$ and Fe $2p_{3/2}$, respectively [27]. Here Fe $2p_{3/2}$ peak can be deconvoluted into peaks located at 711.7 eV and 709.9 eV, corresponding to Fe^{3+} and Fe^{2+} as expected [28]. Moreover, there is no peak observed at about 719 eV, which is usually considered as the fingerprint of γ-Fe_2O_3 [29], suggesting that the as-deposited Fe_3O_4 is phase pure. More XPS results can be found in Fig. S2. Furthermore, the ordered Fe_3O_4 nanodots are examined by SEM images with EDS mappings in Fig. S3, again showing

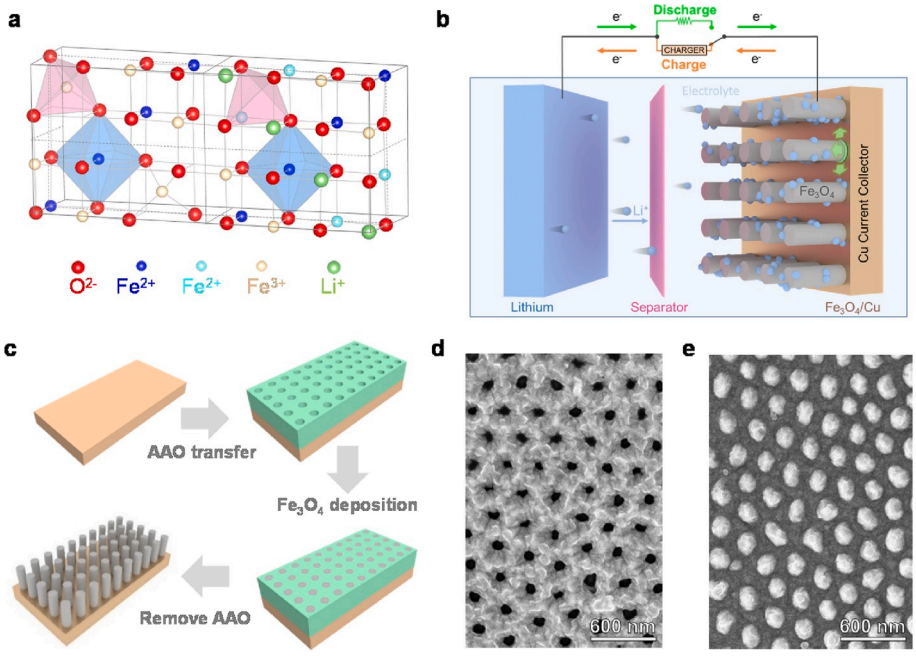

Fig. 1. Deposition of Fe_3O_4 array for LIBs. (a) Structure of Fe_3O_4 unit cell (left panel) and its evolved structure after lithium intercalation (right panel); (b) Schematic of LIBs based on Fe_3O_4 array; (c) Flowchart of epitaxial Fe_3O_4 array deposition on Cu foil using AAO template; (d,e) Top-view SEM images of Fe_3O_4 array before (d) and after (e) removal of AAO mask.

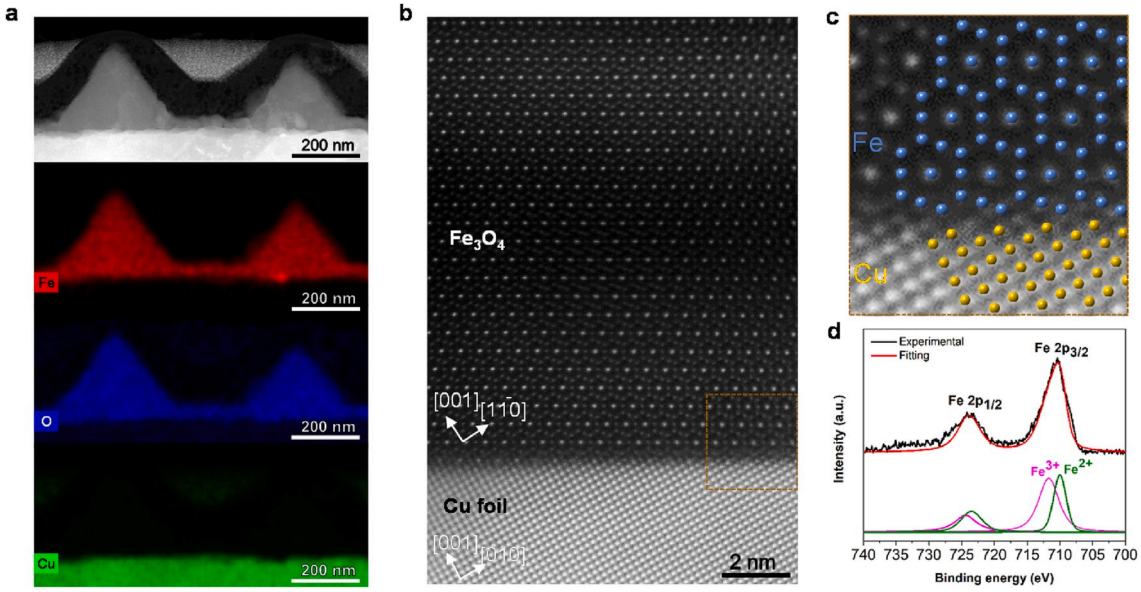

Fig. 2. Structure of as-deposited Fe_3O_4 array. (a) Cross-sectional STEM image of Fe_3O_4 array with elemental mappings of Fe, O and Cu; (b) Atomically resolved HAADF-STEM image at the interface between Fe_3O_4 nanodot and Cu foil substrate; (c) HAADF-STEM image at selected region of Cu–Fe_3O_4 interface. Overlaid structural models identify the Fe_3O_4 and Cu atomic columns. Fe and Cu atomic columns are shown in blue and yellow, respectively. The oxygen atoms are not shown for clarity; (d) XPS of Fe 2p from Fe_3O_4 array. (For interpretation of the references to colour in this figure legend, the reader is referred to the Web version of this article.)

uniform distribution of Fe and O in the nanodots. These microscopic and spectroscopic data thus confirm the high quality phase pure Fe_3O_4 array on Cu foil.

The electrochemical performance of Fe_3O_4 array in comparison with Fe_3O_4 film as anode material in LIBs are studied in Fig. 3. Cyclic Voltammetry (CV) curves of Fe_3O_4 array with scanning rate of 0.1 mV/s in the first four cycles are examined in Fig. 3a, where the cathodic peak located at 0.94 V reveals the reduction of Fe^{3+}/Fe^{2+} to Fe^0 process, as commonly reported in the literature [30,31], and more refined reduction steps cannot be resolved by CV due to their small difference [13]. The small reduction peak at 1.56 V in the first cycle can be attributed to the formation of solid electrolyte interface (SEI) [32]. For the anodic process, there are two peaks located at around 1.63 V and 1.77 V, corresponding to the oxidation of Fe^0 to Fe^{2+} and Fe^{3+}, respectively [33]. Noting that these CV curves from 2nd to 4th cycles overlap with each other well, indicting reversible and stable cyclic performance of epitaxial Fe_3O_4 array under the small scanning rate. Galvanostatic discharge-charge voltage profiles of Fe_3O_4 array at a current density of 5C are presented in Fig. 3b. The voltage plateau of first discharge curve is located at about 0.76 V, which is smaller than that of other cycles at about 1.0 V, and this can be attributed to the formation of SEI layer [32]. The initial discharge-charge specific capacities are measured to be 1350 mA h/g and 1106 mA h/g, respectively, corresponding to a columbic efficiency of 85%. It is quite high for the initial columbic efficiency, suggesting less irreversible electrochemical reaction in SEI layer, which is attributed to the well-ordered nanodot array with large specific surface area that facilitates rapid formation of stable SEI layer [34]. The discharge specific capacities of 2nd and 3rd cycles drop to 935.6 mA h/g and 891.3 mA h/g, and with further cycling, the specific capacity decreases gradually, reaches about 550 mA h/g at 100th cycle and

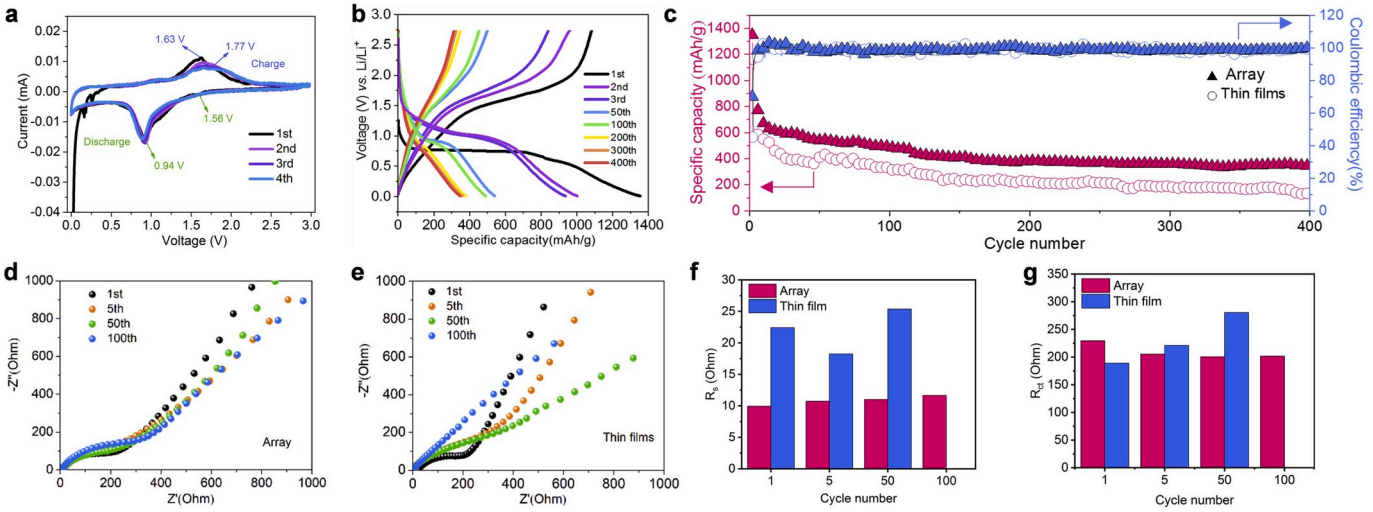

Fig. 3. Electrochemical performance of Fe_3O_4-based LIBs. (a) CV curves of the first four cycles of Fe_3O_4 array; (b) Galvanostatic discharge-charge voltage profiles with a current density of 5C for different cycles; (c) Cyclic performance of Fe_3O_4 array and film under a current density of 5C; (d,e) Nyquist plots of the AC impedance for 1st, 5th, 50th, and 100th cycles of Fe_3O_4 array (d) and film (e); and (f,g) the comparisons of the corresponding R_S (f) and R_{CT} (g).

maintains 350 mA h/g at 400th cycle. As a result, Fe_3O_4 array exhibits relatively stable performance with long cycling life for LIBs under a pretty high current of 5C, as shown in Fig. 3c, wherein data for Fe_3O_4 film is also presented. In comparison, Fe_3O_4 film delivers initial discharge and charge specific capacity of 1164 mA h/g and 526 mA h/g, respectively, corresponding to a columbic efficiency of only 45%. Subsequently, Fe_3O_4 film exhibits a capacity of 330 mA h/g and 123 mA h/g at 100th and 400th cycles, which are much smaller than those of Fe_3O_4 array, with faster decay.

To better understand the enhanced specific capacity with good cyclic stability of Fe_3O_4 array, electrochemical impedance spectroscopy (EIS) of Fe_3O_4 array and film at the 1st, 2nd, 50th, and 100th cycles are studied in Fig. 3d and e, respectively. One depressed semi-circles in the high frequency regions are observed in the Nyquist plots of both array and film (1st cycle), though it becomes linear for Fe_3O_4 film at 100th cycles. It is also evident that Fe_3O_4 array possesses much smaller impedance than that of film, as shown by the comparisons of fitting parameters plotted in Fig. 3f and g, extracted from an equivalent circuit shown in Fig. S4. Here R_S represents the contact and solution resistance in the high-frequency region, while R_{CT} denotes charge transfer resistance in the middle-frequency region [35]. It is observed that R_S of Fe_3O_4 array is not only much smaller because of its larger specific surface area, but also more stable with cycling, increasing from 9.9 Ω in the first cycle to 11.7 Ω at the 100th cycles, respectively. R_S of Fe_3O_4 film, on the other hand, increases from 22.4 Ω in the first cycle to 25.4 Ω at 50th cycle, and the spectroscopy becomes linear at 100th cycle, indicating that Li^+ diffusion process becomes dominant during the electrochemical process [36]. Furthermore, R_{CT} of Fe_3O_4 array is 229.4 Ω in the first cycle, and then decreases to 205.3 Ω, 200.6 Ω, 201.8 Ω at 5th, 50th, and 100th cycles, which is attributed to the enhanced electrochemical activity of Fe_3O_4 array after the formation of stable SEI layer at 1st cycle. The relatively stable R_{CT} also indicates reversible expansion and shrinkage of electrode during conversion-type electrochemical reaction. R_{CT} of Fe_3O_4 film, on the other hand, is 188.9 Ω at first cycle, and increases to 221 Ω and 280.6 Ω at 5th and 50th cycles, indicating irreversibility of electrochemical reaction, which is believed to be caused by SEI formation and electrode damage [37]. These results indicate that well-ordered Fe_3O_4 array possesses stable structure and electrode/electrolyte interface for enhanced cycling performance.

In addition to cyclability at a high current density, Fe_3O_4 array also displays remarkably high rate capability, as shown in Fig. 4a in comparison to Fe_3O_4 film. The Fe_3O_4 array/film delivers specific capacities of 529.1/607.7, 561.6/618.8, 550.1/552.6, 501.5/424.8, 406.5/288.4 and 312.5/222.3 mA h/g at current densities of 1, 2, 5, 10, 30 and 60C, respectively. Notice that the specific capacities of these two types of electrodes are similar at 1, 2, and 5C with those of film electrode slightly higher, yet at high current densities of 30 and 60C, Fe_3O_4 array exhibits much larger capacity than film. Furthermore, Fe_3O_4 array/film maintain reversible specific capacity of 444.3/418.4, 366/275.7, 550.6/364.8 and 487.5/302.6 mA h/g under current densities of 5, 10, 2, and 5C tested between 100th and 140th cycles, after which Fe_3O_4 array delivers a high specific capacity of 427.5 mA h/g up to 180 cycles at 10C. Fe_3O_4 film, on the other hand, maintains a specific capacity of only 164.6 mA h g^{-1} at 180 cycles under 10C. More comparisons for Fe_3O_4 arrays with different diameters are shown in Fig. S5, all of which exhibits good rate capability, while 130 nm is optimal among the systems we studied.

Galvanostatic discharge-charge voltage profiles of Fe_3O_4 in different cycles under 2C are presented in Fig. 4b. Note that the discharge-charge specific capacity of Fe_3O_4 array shows small change within a narrow range between 600 mA h/g to 540 mA h/g at 15th, 95th, and 125th cycles, yet substantial specific capacity difference can be found for Fe_3O_4 film. The much enhanced rate capability of Fe_3O_4 array can be understood from SEM images of Fe_3O_4 array and film after 100 cycles under an ultrahigh current density of 60C shown in Fig. 4c and d. While cracks clearly develop in Fe_3O_4 film, the structure of well-ordered nanodot array is maintained after long cycling under such a high current density. This is attributed to the spaced nanodot array that can effectively accommodate volume expansion and contraction during Li^+ insertion/deinsertion [38,39]. The well-ordered Fe_3O_4 array having tight contact with Cu foil current collect provides rapid electronic transport route, ideal for high rate applications. We also compare electrochemical performance of various nanostructured Fe_3O_4 for LIBs [18–21,31,40–52] in Fig. 4e, from which it is evident that our phase pure Fe_3O_4 array clearly stands out and outperforms other composite

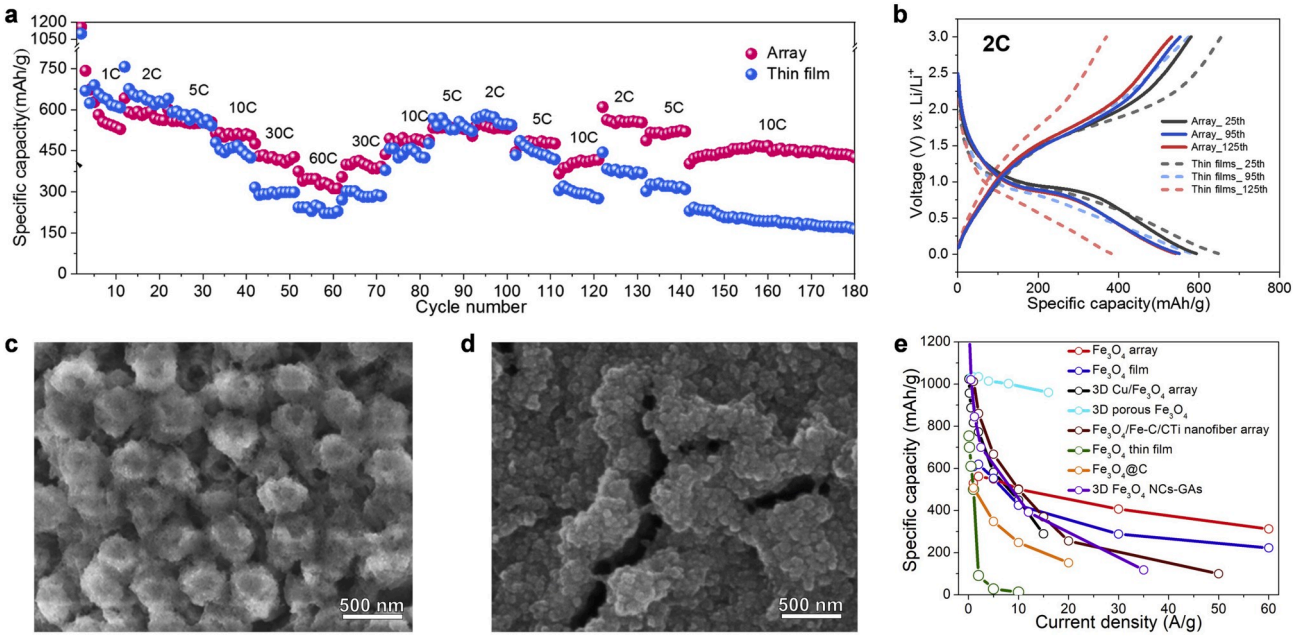

Fig. 4. Rate performance of Fe_3O_4 array and film. (a) Rate capability of Fe_3O_4 array and film; (b) Galvanostatic discharge-charge voltage profiles of different cycles at a current density of 2C; (c,d) Top-view SEM images of Fe_3O_4 array (c) and film (d) after 100 cycles at a ultrahigh current density of 60C; (e) Comparison of electrochemical performance for Fe_3O_4 based electrodes as anode material for LIBs.

systems, especially under high current rate.

The outstanding electrochemical performance of Fe_3O_4 array, especially under high current density, can be attributed to its structural stability during Li^+ insertion and deinsertion. To appreciate this, we carry out detailed structure analysis at charged and discharged stages after cycling. Charged Fe_3O_4 array after 10 cycles is examined in Fig. 5a–d, where the cross-sectional STEM image in Fig. 5a clearly reveals one independent nanodot on Cu foil, confirming that the structure of Fe_3O_4 array is largely maintained after cycling. The SAED pattern in Fig. 5b obtained from the nanodot can be determined as from Fe_3O_4 phase. The EDS mappings in Fig. 5c reveal the uniform distribution of Fe and O elements in the nanodot, showing good interface with Cu maintained, and more data can be found in Figs. S6a–d. The atomic structure of charged nanodot is revealed by STEM image in Fig. 5d, confirming its Fe_3O_4 phase. It should be noted that in addition to Fe_3O_4, $Li_xFe_3O_4$ and FeO are also observed, with more information in Figs. S6f–g, consistent with previous reports on conversion-type electrodes [17]. Regarding the discharged stage, we examine Fe_3O_4 array after 50 cycles. The nanodot structure of Fe_3O_4 is largely maintained as shown in Fig. 5e and Figs. S7a and b. More importantly, the Fe and Li_2O phases are clearly observed in Fig. 5f, though there are also Fe_3O_4 phase remaining, suggesting some irreversible/incomplete reactions. EDS mappings in Fig. 5g and electron energy loss spectroscopy (EELS) mappings in Fig. S7c confirm the uniform distribution of Fe, O, Li elements in nanodot and well-maintained interface at discharged stage. Furthermore, detailed atomic structure in Fig. 5h and Figs. S7d and e confirm the existence of Fe and Fe_3O_4 phase in the nanodot after discharging. These systematic studies on the detailed structure evolution of Fe_3O_4 array at charged and discharged stages after cycling not only demonstrate the structure stability of Fe_3O_4 after cycled Li^+ insertion/deinsertion, but also confirm good electrochemical activity of Fe_3O_4 electrode under both charge and discharge processes.

Recently, it has been reported that the formation and accumulation of a passivation layer, verified to be the products of conversion reaction, Li_2O, is responsible for the poor cyclic and rate performance of conversion-type electrode [17]. While the formation of metallic nanoparticles improves the electronic conductivity, the rapid accumulation of Li_2O between metallic nanoparticles functions as a passivation layer, gradually impeding electrochemical reactions due to its poor electronic conductivity. To examine this effect in our Fe_3O_4 nanodot, we analyze HAADF-STEM images of Fe_3O_4 array after 10 cycles and 50 cycles as shown in Fig. 6a and b. The nanoparticles with bright contrast correspond to the iron or iron oxides, while the dark gap is considered to be Li_2O phase based on previous report [17,53]. To facilitate quantitative comparison, the distributions of particle size and gap between particles are extracted from the STEM images after 10 cycles and 50 cycles as shown in Fig. 6c and d, obtained from different regions over 1.2×10^4 nm^2 including the regions shown in Fig. 6a and b and representative regions in Fig. S8. While data for 50 cycles become more scattering with increased numbers for larger particle size and gap, the average particle size only increases slightly, from 3.60 nm after 10 cycles to 3.62 nm after 50 cycles. Similar trend is also observed for gap between particles, increasing from 2.31 nm after 10 cycles to 2.34 nm after 50 cycles, indicating rather slow accumulation of passivation layers with increased electrochemical cycles. Note that the particle size is much smaller than previous report of approximately 8–10 nm [17,54], and very few large particles around 10 nm can be found after 50 cycles, and thus the growth of internal passivation is also much slower than previous report. These detailed microstructural study thus shed further light into the outstanding electrochemical performance of Fe_3O_4 array electrode. In particular, not only the global array structure of Fe_3O_4 is largely intact upon cycling, but also the local phase microstructure is stable, with much slower augmentation of the passivation layers.

3. Conclusion

In summary, epitaxial array of Fe_3O_4 nanodots has been deposited on Cu foils by AAO-assisted PLD, resulting binder-free conversion electrode

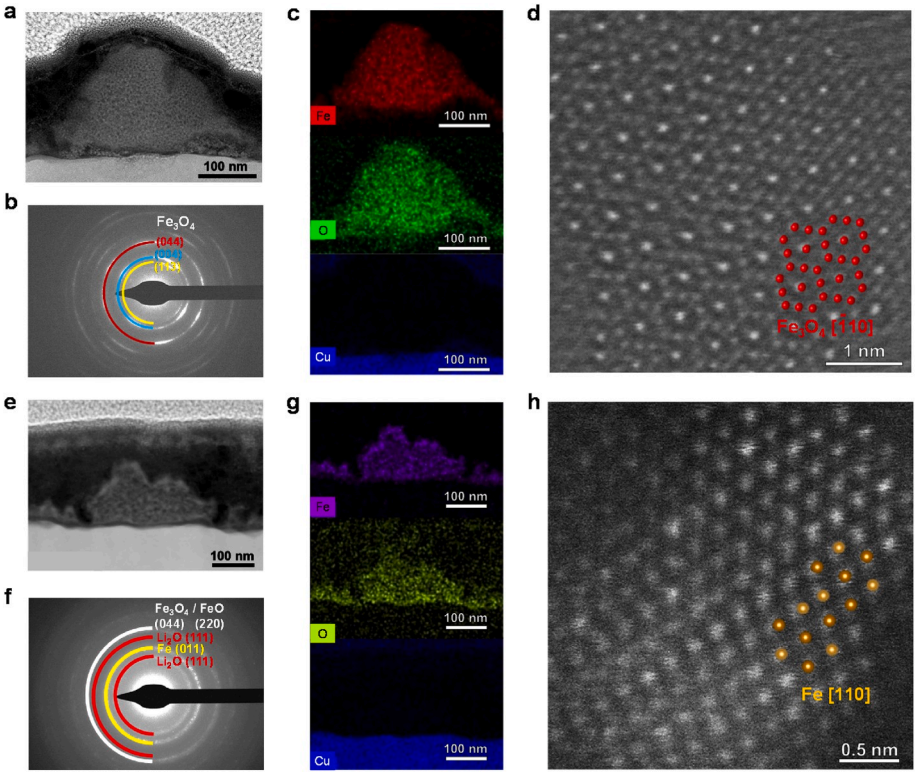

Fig. 5. Phase evolution of Fe_3O_4 array during cycling. (a–d) STEM image, SAED pattern, EDS mappings and atomic-resolution HAADF-STEM image of charged Fe_3O_4 array after 10 cycles; (e–h) STEM image, SAED pattern, EDS mappings and atomic-resolution HAADF-STEM image of discharged Fe_3O_4 array after 50 cycles.

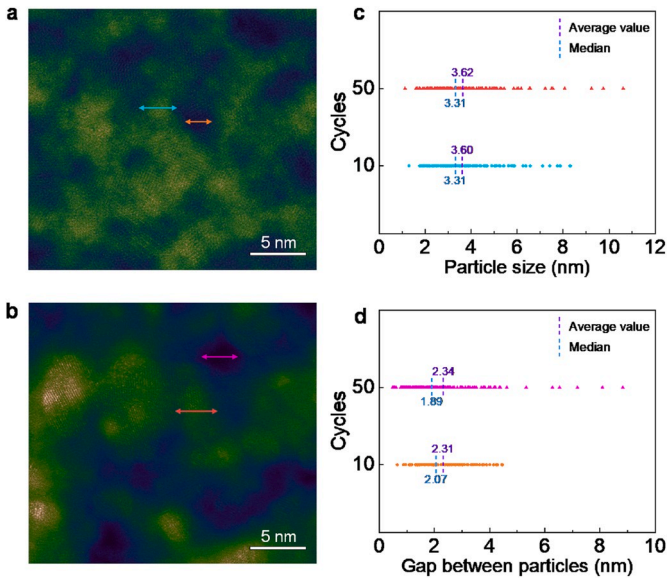

Fig. 6. Microstructural evolution of Fe_3O_4 array during cycling. (a,b) Typical HAADF-STEM morphology of Fe_3O_4 array electrode after 10 cycles charged (a) and 50 cycles discharged (b). The double-headed arrow is used to mark the particles with bright contrast and the gap between fine particles with dark contrast. (c,d) The distributions of particle size and the gap between fine particles extracted from the STEM images of Fe_3O_4 array electrode after 10 cycles (c) and 50 cycles (d) over 1.2×10^4 nm^2.

in LIBs with remarkably high rate capability and long cycling life. For conventional conversion-type electrodes, the rapid capability fading is usually caused the materials breakdown, contact failure, and internal passivation, while our Fe_3O_4 array electrode address these three issues comprehensively, rendering new insight into optimizing conversion electrodes for practical applications.

Declaration of competing interest

The authors declare no conflict of interests.

CRediT authorship contribution statement

Gaokuo Zhong: Conceptualization, Data curation, Funding acquisition, Investigation, Writing - original draft, Writing - review & editing. **Ke Qu:** Data curation, Investigation. **Chuanlai Ren:** Data curation, Investigation. **Yong Su:** Investigation. **Bi Fu:** Investigation, Writing - original draft. **Mengfei Zi:** Investigation. **Liyufen Dai:** Investigation. **Qun Xiao:** Investigation. **Jun Xu:** Investigation. **Xiangli Zhong:** Investigation. **Feng An:** Investigation. **Mao Ye:** Investigation. **Shanming Ke:** Investigation. **Shuhong Xie:** Investigation. **Jinbin Wang:** Investigation. **Peng Gao:** Data curation, Funding acquisition, Investigation, Project administration, Supervision. **Jiangyu Li:** Conceptualization, Funding acquisition, Project administration, Supervision, Writing - original draft, Writing - review & editing.

Acknowledgement

We acknowledge National Natural Science Foundation of China (51902337, 11875229, 51872251, 51672007, 11974023), National Key Research and Development Program of China (2016YFA0201001), Shenzhen Science and Technology Innovation Committee (KQTD20170810160424889, JCYJ20170818155813437) and Key-Area Research and Development Program of Guang Dong Province (No. 2018B030327001).

Appendix A. Supplementary data

Supplementary data to this article can be found online at https://doi.org/10.1016/j.nanoen.2020.104876.

References

[1] G.-L. Xu, et al., Building ultraconformal protective layers on both secondary and primary particles of layered lithium transition metal oxide cathodes, Nat. Energy 4 (2019) 484–494.
[2] M. Armand, J.-M. Tarascon, Building better batteries, Nature 451 (2008) 652–657.
[3] P. Albertus, S. Babinec, S. Litzelman, A. Newman, Status and challenges in enabling the lithium metal electrode for high-energy and low-cost rechargeable batteries, Nat. Energy 3 (2018) 16–21.
[4] P. Poizot, S. Laruelle, S. Grugeon, L. Dupont, J.-M. Tarascon, Nano-sized transition metal oxide as negative-electrode materials for lithium-ion batteries, Nature 407 (2000) 496–499.
[5] S.-H. Yu, S.H. Lee, D.J. Lee, Y.-E. Sung, T. Hyeon, Conversion reaction-based oxide nanomaterials for lithium ion battery anodes, Small 12 (2016) 2146–2172.
[6] F. Wu, G. Yushin, Conversion cathodes for rechargeable lithium and lithium-ion batteries, Energy Environ. Sci. 10 (2017) 435–459.
[7] P.L. Taberna, S. Mitra, P. Poizot, P. Simon, J.-M. Tarascon, High rate capabilities Fe_3O_4-based Cu nano-architectured electrodes for lithium-ion battery applications, Nat. Mater. 5 (2006) 567–573.
[8] Y. Liu, Y. Zhu, Y. Cui, Challenges and opportunities towards fast-charging battery materials, Nat. Energy 4 (2019) 540–550.
[9] W. Zhang, et al., Insights into ionic transport and structural changes in magnetite during multiple-electron transfer reactions, Adv. Energy Mater. 6 (2016) 1502471.
[10] S. Hwang, et al., Strain coupling of conversion-type Fe_3O_4 thin films for lithium ion batteries, Angew. Chem. Int. Ed. 56 (2017) 7813–7816.
[11] A.M. Bruck, et al., Temporally and spatially resolved visualization of electrochemical conversion: monitoring phase distribution during lithiation of magnetite (Fe_3O_4) electrodes, ACS Appl. Energy Mater. 2 (2019) 2561–2569.
[12] M.M. Thackeray, W.I.F. David, J.B. Goodenough, Structural characterization of the lithiated iron oxides $Li_xFe_3O_4$ and $Li_xFe_2O_3$ ($0< x< 2$), Mater. Res. Bull. 17 (1982) 785–793.
[13] M.M. Thackeray, J. Coetzer, A preliminary investigation of the electrochemical performance of α- Fe_2O_3 and Fe_3O_4 cathodes in high-temperature cells, Mater. Res. Bull. 16 (1981) 591–597.
[14] F.X. Ma, et al., Formation of uniform Fe_3O_4 hollow spheres organized by ultrathin nanosheets and their excellent lithium storage properties, Adv. Mater. 27 (2015) 4097–4101.
[15] Z. Yang, D. Su, J. Yang, J. Wang, et al., Fe_3O_4/C composite with hollow spheres in porous 3D-nanostructure as anode material for the lithium-ion batteries, J. Power Sources 363 (2017) 161–167.
[16] X. Xu, et al., Facile synthesis of three-dimensional Cu/Fe_3O_4 nanowires as binder-free anode for lithium-ion batteries, Appl. Surf. Sci. 450 (2018) 356–363.
[17] J. Li, et al., Phase evolution of conversion-type electrode for lithium ion batteries, Nat. Commun. 10 (2019) 2224.
[18] Y. Liu, et al., Fe_3O_4 quantum dots embedded in porous carbon microspheres for long-life lithium-ion batteries, Mater. Today Energy 12 (2019) 269–276.
[19] R. Ding, et al., N-doped dual carbon-confined 3D architecture rGO/Fe_3O_4/AC nanocomposite for high-performance lithium-ion batteries, ACS Appl. Mater. Interfaces 10 (2018) 13470–13478.
[20] L. Fan, B. Li, D.W. Rooney, N. Zhang, K. Sun, In situ preparation of 3D graphene aerogels@hierarchical Fe_3O_4 nanoclusters as high rate and long cycle anode materials for lithium ion batteries, Chem. Commun. 51 (2015) 1597–1600.
[21] P. Zhang, W. Yue, R. Li, Uniform yolk-shell Fe_3O_4@nitrogen-doped carbon composites with superior electrochemical performance for lithium-ion batteries, Electrochim. Acta 282 (2018) 595–601.
[22] W. Zhang, et al., Multi-electron transfer enabled by topotactic reaction in magnetite, Nat. Commun. 10 (2019) 1972.
[23] G. Zhong, et al., Deterministic, reversible, and nonvolatile low-voltage writing of magnetic domains in epitaxial $BaTiO_3$/Fe_3O_4 heterostructure, ACS Nano 12 (2018) 9558–9567.
[24] M.M. Thackeray, Spinel electrodes for lithium batteries, J. Am. Ceram. Soc. 82 (1999) 3347–3354.
[25] Y. Sun, N. Liu, Y. Cui, Promises and challenges of nanomaterials for lithium-based rechargeable batteries, Nat. Energy 1 (2016) 16071.
[26] W. Lee, et al., Individually addressable epitaxial ferroelectric nanocapacitor arrays with near Tb $inch^{-2}$ density, Nat. Nanotechnol. 3 (2008) 402.
[27] F. Han, L. Ma, Q. Sun, C. Lei, A. Lu, Rationally designed carbon-coated Fe_3O_4 coaxial nanotubes with hierarchical porosity as high-rate anodes for lithium ion batteries, Nano Res. 7 (2014) 1706–1717.
[28] J. He, et al., Graphene-doped carbon/Fe_3O_4 porous nanofibers with hierarchical band construction as high-performance anodes for lithium-ion batteries, Electrochim. Acta 229 (2017) 306–315.
[29] J. Wang, et al., A platinum anticancer theranostic agent with magnetic targeting potential derived from maghemite nanoparticles, Chem. Sci. 4 (2013) 2605–2612.
[30] Y. Huang, et al., Revisiting the origin of cycling enhanced capacity of Fe_3O_4 based nanostructured electrode for lithium ion batteries, Nano Energy 41 (2017) 426–433.
[31] M. Liu, et al., One-pot synthesis of in-situ carbon-coated Fe_3O_4 as a long-life lithium-ion battery anode, Nanotechnology 28 (2017) 155603.

[32] S. Chen, et al., Sea-sponge-like structure of nano-Fe_3O_4 on skeleton-C with long cycle life under high rate for Li-ion batteries, ACS Appl. Mater. Interfaces 10 (2018) 19656–19663.
[33] L. Li, et al., Enhanced cycling stability of lithium-ion batteries using graphene-wrapped Fe_3O_4-graphene nanoribbons as anode materials, Adv. Energy Mater. 5 (2015) 1500171.
[34] H. Ye, S. Xin, Y.X. Yin, Y.G. Guo, Advanced porous carbon materials for high-efficient lithium metal anodes, Adv. Energy Mater. 7 (2017) 1700530.
[35] E. Barsoukov, J.R. Macdonald (Eds.), Impedance Spectroscopy: Theory, Experiment, and Applications, John Wiley & Sons, 2018.
[36] S.S. Zhang, K. Xu, T.R. Jow, EIS study on the formation of solid electrolyte interface in Li-ion battery, Electrochim. Acta 51 (2006) 1636–1640.
[37] C. Zhang, T.H. Kang, J.S. Yu, Three-dimensional spongy nanographene-functionalized silicon anodes for lithium ion batteries with superior cycling stability, Nano Res. 11 (2018) 233–245.
[38] C.K. Chan, et al., High-performance lithium battery anodes using silicon nanowires, Nat. Nanotechnol. 3 (2008) 31.
[39] C. Wang, et al., Carbon-modified $Na_2Ti_3O_7{\cdot}2H_2O$ nanobelts as redox active materials for high-performance supercapacitor, Nano Energy 28 (2016) 115–123.
[40] H. Qi, et al., Rice crust-like Fe_3O_4@C/rGO with improved extrinsic pseudocapacitance for high-rate and long-life Li-ion anodes, J. Alloys Compd. 804 (2019) 57–64.
[41] X. Fan, S. Li, H. Zhou, L. Lu, One-pot high temperature hydrothermal synthesis of Fe_3O_4@C/graphene nanocomposite as anode for high rate lithium ion battery, Electrochim. Acta 180 (2015) 1041–1049.
[42] W. Han, et al., Electrosprayed porous Fe_3O_4/carbon microspheres as anode materials for high-performance lithium-ion batteries, Nano Res. 11 (2018) 892–904.
[43] S. Huang, et al., Inward lithium-ion breathing of hollow carbon spheres-encapsulated Fe_3O_4@C nanodisc with superior lithium ion storage performance, J. Alloys Compd. 800 (2019) 16–22.
[44] C. Liao, S. Wu, Pseudocapacitance behavior on Fe_3O_4-pillared SiO_x microsphere wrapped by graphene as high performance anodes for lithium-ion batteries, Chem. Eng. J. 355 (2019) 805–814.
[45] Q. Wu, et al., Synthesis of flexible Fe_3O_4/C nanofibers with buffering volume expansion performance and their application in lithium-ion batteries, J. Power Sources 359 (2017) 7–16.
[46] Y. Yang, J. Li, D. Chen, J. Zhao, A facile electrophoretic deposition route to the Fe_3O_4/CNTs/rGO composite electrode as a binder-free anode for lithium ion battery, ACS Appl. Mater. Interfaces 8 (2016) 26730–26739.
[47] W. Zhang, et al., One-step thermolysis synthesis of two-dimensional ultrafine Fe_3O_4 particles/carbon nanonetworks for high-performance lithium-ion batteries, Nanoscale 8 (2016) 4733–4741.
[48] Z.W. Zhao, et al., Carbon-coated Fe_3O_4/VO_x hollow microboxes derived from metal-organic frameworks as a high-performance anode material for lithium-ion batteries, ACS Appl. Mater. Interfaces 9 (2017) 3757–3765.
[49] Q. Zhao, et al., Novel in-situ redox synthesis of Fe_3O_4/rGO composites with superior electrochemical performance for lithium-ion batteries, Electrochim. Acta 262 (2018) 233–240.
[50] S. Zhou, et al., Synthesis of Fe_3O_4 cluster microspheres/graphene aerogels composite as anode for high-performance lithium ion battery, Appl. Surf. Sci. 439 (2018) 927–933.
[51] B. Zhu, et al., Preparation of dual layers N-doped carbon@mesoporous carbon@Fe_3O_4 nanoparticle superlattice and its application in lithium-ion battery, J. Alloys Compd. 775 (2019) 776–783.
[52] Y. Zuo, et al., Hybridization of graphene nanosheets and carbon-coated hollow Fe_3O_4 nanoparticles as a high-performance anode material for lithium-ion batteries, J. Mater. Chem. 4 (2016) 2453–2460.
[53] Y.X. Chen, et al., Micro-sized and nano-sized Fe_3O_4 particles as anode materials for lithium-ion batteries, J. Mater. Sci. Technol. 27 (2011) 41–45.
[54] S.H. Lee, et al., Self-assembled Fe_3O_4 nanoparticle clusters as high-performance anodes for lithium ion batteries via geometric confinement, Nano Lett. 13 (2013) 4249–4256.

Dr. Gaokuo Zhong received his Ph.D. degree in Materials Science and Engineering from Xiangtan University in 2018. Now, he is an associate professor in Shenzhen Institutes of Advanced Technology, Chinese Academy of Sciences. His research focuses on the ferroelectric materials, multiferroics and flexible electronics.

Dr. Ke Qu received her Ph.D. degree in Condensed Matter Physics from Lanzhou University in 2018. Now, she has joined Shenzhen Institutes of Advanced Technology, Chinese Academy of Sciences, as a postdoctoral. Her research focuses on the atomic resolution structure and electronic structure evolution of transition metal oxides in-situ Cs-corrected transmission electron microscopy.

Chuanlai Ren is a Ph.D. candidate in Materials Science and Engineering at Xiangtan University. His research interest focuses on ferroelectric materials and flexible electronics.

Yong Su is a Ph.D. candidate in Materials Science and Engineering at Xiangtan University. His research interest focuses on energy storage materials.

Dr. Bi Fu received his Ph.D. degree in Physics from Xi'an Jiaotong University in 2016. He is a research Assistant in Shenzhen Institutes of Advanced Technology, Chinese Academy of Sciences. His research focuses on the material physics and advanced functional materials.

Mengfei Zi is a master degree candidate in Materials Science and Engineering at Xiangtan University. His research interest focuses on multiferroics and flexible electronics.

Liyufen Dai is a master degree candidate in Materials Science and Engineering at Xiangtan University. Her research interest focuses on energy materials.

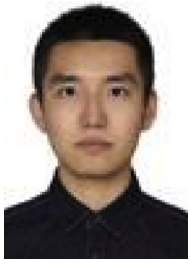

Qun Xiao is a master degree candidate in Materials Science and Engineering at Xiangtan University. His research interest focuses on scanning probe microscopy.

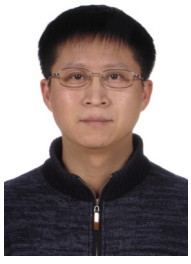

Jun Xu is a Professor-level Senior engineer in Electron Microscopy Lab., School of Physics, Peking University, Beijing, China. He joined in Peking University in 1988. His research interests include electron microscopy, focused ion beam, electron beam lithography and cathodoluminescence spectrum analysis.

Dr. Xiangli Zhong received her Ph.D. degree in materials physics and chemistry from Xiangtan University in 2008. She is a professor in Xiangtan University. Her research interests include ferroelectric thin-film memory and other advanced complementary metal–oxide–semiconductor devices.

Feng An is a Ph.D. candidate in Materials Science and Engineering at Xiangtan University. His research interest focuses on multiferroics and flexible electronics.

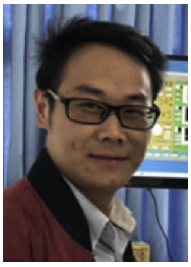

Dr. Mao Ye received his Ph.D. degree in Chemical Engineering and Technology from Harbin Institute of Technology University in 2013. He is a research assistant professor in South University of Science and Technology of China. His research focuses on the ferroelectric materials, complex functional oxide film and flexible electronics.

Dr. Shanming Ke received his Ph.D. degree in Materials Science from Northwestern Polytechnical University in 2008. Now, he has joined Nanchang University, as a professor. His research focuses on the ferroelectric materials, complex functional oxide film and nano-photoelectron material.

Dr. Shuhong Xie received her Ph.D. degree in Materials and physical chemistry from Xiangtan University in 2008. She is a professor in Xiangtan University. Her research focuses on the multiferroics and thermoelectric materials.

Dr. Jinbin Wang received his Ph.D. degree in microelectronics and solid-state electronics from Shanghai Institute of Technical Physics, Chinese Academy of Sciences, Shanghai, China, in 2005. He is a Professor in Xiangtan University. His research interests include semiconductors and their devices, the growth of thin films.

Peng Gao is an assistant Professor in School of Physics, Peking University, Beijing, China. He received his Ph.D. degree in condensed mater physics from the Institute of Physics, Chinese Academy of Sciences in 2010. He was a postdoctor in University of Michigan (2010–2013), research associate in Brookhaven National Lab (2013–2014), research fellow and Japan Society for the Promotion of Science (JSPS) foreign fellow in University of Tokyo (2014–2015). He joined in Peking University in 2015. His research interests include electron microscopy, ferroelectrics, solid-state ionics, and structure and properties of crystal defects and interfaces.

Dr. Jiangyu Li obtained his B.E. degree in 1994 from the Department of Materials Science and Engineering, Tsinghua University, and Ph.D. degree in 1998 from the Department of Mechanical Engineering, He recently joins Shenzhen Institutes of Advanced Technology, Chinese Academy of Sciences. He works in the general field of mechanical of materials, focusing on advanced scanning probe microscopy and its applications in functional materials.